# Measuring Physical Properties of Neuronal and Glial Cells with Resonant Microsensors

Elise A. Corbin,[†,‡] Larry J. Millet,[‡,§,⊥] Katrina R. Keller,[‡,∥] William P. King,[†,‡] and Rashid Bashir*[,‡,∥,⊥]

[†]Department of Mechanical Engineering, University of Illinois Urbana−Champaign, Urbana, Illinois 61801, United States
[‡]Micro and Nanotechnology Laboratory, University of Illinois Urbana−Champaign, Urbana, Illinois 61801, United States
[§]Neuroscience Program, University of Illinois Urbana−Champaign, Urbana, Illinois 61801, United States
[∥]Department of Bioengineering, University of Illinois Urbana−Champaign, Urbana, Illinois 61801, United States
[⊥]Department of Electrical and Computer Engineering, University of Illinois Urbana−Champaign, Urbana, Illinois 61801, United States

**ABSTRACT:** Microelectromechanical systems (MEMS) resonant sensors provide a high degree of accuracy for measuring the physical properties of chemical and biological samples. These sensors enable the investigation of cellular mass and growth, though previous sensor designs have been limited to the study of homogeneous cell populations. Population heterogeneity, as is generally encountered in primary cultures, reduces measurement yield and limits the efficacy of sensor mass measurements. This paper presents a MEMS resonant pedestal sensor array fabricated over through-wafer pores compatible with vertical flow fields to increase measurement versatility (e.g., fluidic manipulation and throughput) and allow for the measurement of heterogeneous cell populations. Overall, the improved sensor increases capture by 100% at a flow rate of 2 $\mu$L/min, as characterized through microbead experiments, while maintaining measurement accuracy. Cell mass measurements of primary mouse hippocampal neurons in vitro, in the range of 0.1−0.9 ng, demonstrate the ability to investigate neuronal mass and changes in mass over time. Using an independent measurement of cell volume, we find cell density to be approximately 1.15 g/mL.
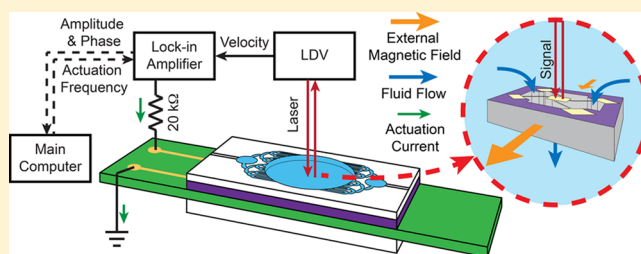
Microelectromechanical systems (MEMS) can accelerate biological and medical research by introducing quantitative measurement devices capable of simultaneously handling, manipulating, and characterizing individual cells.[1] The desire to study the growth of individual cells has driven the development of cantilever,[2] suspended microchannel,[3−5] and pedestal[6,7] resonant sensors, which measure the mass of captured objects through the shift in device resonant frequency. Studies of yeast,[4] human colon cancer cells (HT29),[6] cervical cancer cells (HeLa),[2] and bacterial cells[8] demonstrated that MEMS resonant mass sensors are effective tools for measuring cellular growth rates. Recently, we extended the use of MEMS resonant sensors for the characterization of microscale hydrogel structures for tissue-engineering applications.[9,10]

While cell lines are the population of choice for many cell biology studies, tissue-derived (primary source) cultures are a mainstay for postmitotic cell populations. The process of generating primary, postmitotic neurons in culture yields a highly mixed cellular population, which presents additional challenges for single-cell studies. For over a century, numerous culture devices and methods have provided ideal microenvironments to glean insights into neuronal development.[11−13] MEMS sensor arrays[6,14,15] potentially provide a unique advantage for measuring the growth of neurons, if neurons can be isolated from the heterogeneous population. Neuro-

chemical and cell signaling studies utilize neuronal growth measures in vitro to measure the duration of the polarization process, axonal elongation rates, and filopodial dynamics (space, time, and direction).[16−19] New techniques that allow for additional measures of neuronal growth have the potential to aid in cell signaling studies and investigations into the influence of neurotrophins, cytokines, and neurotoxins on neuronal biomechanics (e.g., stiffness and biomass accumulation).

To enable whole cell mass measurements of target cells within heterogeneous populations for mass and growth analyses, further design requirements and functionalities are required to increase sensor yield. The measurement yield from MEMS resonant pedestal sensors are inherently limited by the presence of objects on the sensor springs, which alters the effective spring constant of the sensor and invalidates the measurement. The stochastic process of random cell seeding in static fluid domains provides a finite limit to the yield; we define sensor yield as the number of functional sensors with appropriately captured objects that provide accurate and

reliable measurements. The measurement yield is further challenged when studying heterogeneous populations as the cells of interest (e.g., neurons) make up only a small fraction of captured objects. To improve the efficiency of our MEMS mass sensor array for heterogeneous populations, we redesigned the fabrication process to incorporate vertical flow fields and on-chip microfluidic channels that remove cells from the sensor springs to increase sensor yield and enable high-throughput growth studies.

This paper reports the design, fabrication, and characterization of a MEMS resonant mass sensor array, where each sensor is suspended over a vertical microfluidic channel etched through the entire silicon wafer. An additional PDMS-based microfluidic perfusion chamber and a backside drainage chamber constitute an on-chip microfluidic system and provide increased functionality. We demonstrate the feasibility of improved capture efficiency through finite element flow simulations and microbead capture experiments. We show that the vertical flow pedestal sensors retain the native functionality of the original, nonflow sensors and use them to measure the mass and growth of mouse primary hippocampal neurons in vitro.

## ■ EXPERIMENTAL SECTION

**Fabrication of Vertical Flow MEMS Resonant Sensor Arrays.** Figure 1 illustrates the key steps of the fabrication
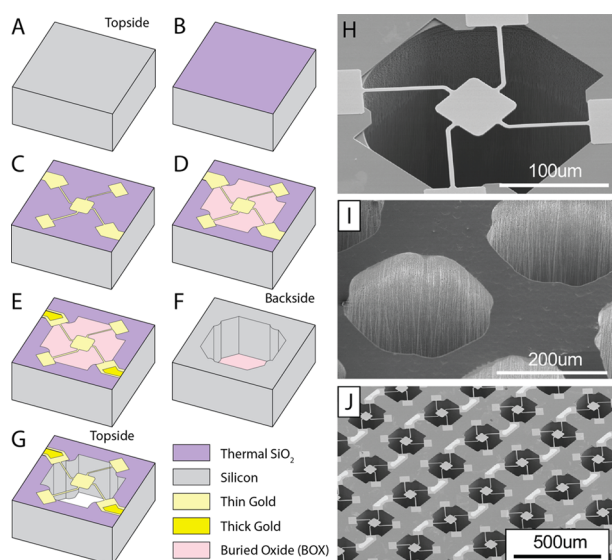


**Figure 1.** (A−G) Fabrication process for vertical flow MEMS mass sensor with backside pore. (H−J) Scanning electron microscope (SEM) images of the resonant mass sensor array.

process, which are outlined here. The starting material was a silicon-on-insulator (SOI) wafer with a 2 $\mu$m thick silicon device layer, a 0.6 $\mu$m buried oxide (BOX) layer, and a 500 $\mu$m silicon handle layer, as depicted in Figure 1A. First, we grew a passivation layer of silicon dioxide (25 nm) using thermal oxidation. After deposition of the passivation layer (Figure 1B), a photolithography process patterned the square pedestals and beam springs. Then, 10 nm of chromium and 50 nm of gold were deposited using thermal evaporation and patterned with a liftoff process. Figure 1C shows the device after the first liftoff process. Once the devices are defined, a photoresist etch mask is patterned by photolithography along with the first metal layer

to create the sensor areas. An inductively coupled plasma (ICP) etcher formed the springs and the platform using the Bosch process, which etched the exposed silicon until it stops at the BOX layer (Figure 1D). A second photolithography patterned the electrodes for connecting the finished devices to printed circuit boards. E-beam evaporation deposited another 100 nm of chromium and 900 nm of gold, which were also patterned through liftoff. Figure 1E shows the resulting metallization of the electrodes, which allows the bias current to flow through a single row of devices at one time.

Fabrication of the backside pore began after metallization. Photolithographic patterning of the wafer backside followed by an ICP etch, again using the Bosch process, removed the 500 $\mu$m silicon handle layer from beneath the platform sensor (Figure 1F). As a result, microfluidic pores with smooth vertical sidewalls were formed in the wafer beneath the sensor structure to permit fluid transport. Next, a buffered oxide etch (BOE) removed the BOX layer, suspending the devices over the backside pore (Figure 1, panels G−J). The final fabrication step deposited a 100 nm silicon dioxide layer for insulation, using a plasma-enhanced chemical vapor deposition (PECVD) process. Prior to wire-bonding the resulting chip to a printed circuit board, we selectively etched the PECVD oxide on the bonding pads with BOE.

**Perfusion Chamber Fabrication and Assembly.** Figure 2A depicts the on-chip microfluidic system that includes a
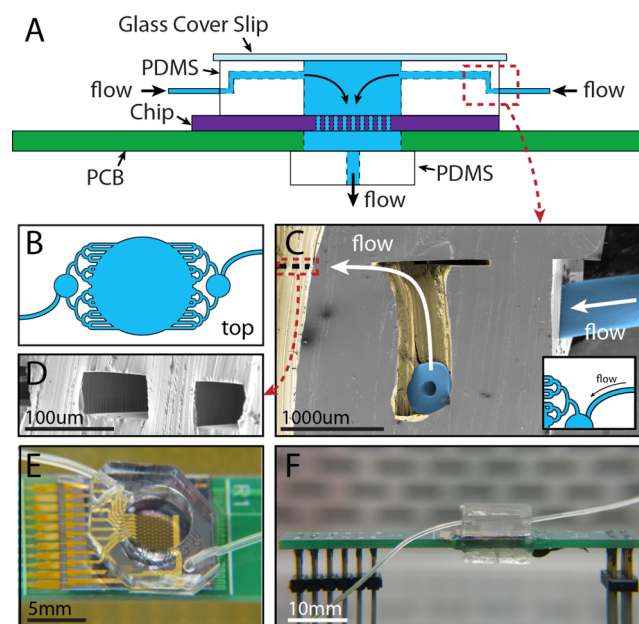


**Figure 2.** Complete chip assembly with microfluidics and fluidic flow description. (A) Schematic of assembled chip showing the PDMS-based microfluidic perfusion layer on chip containing sensor arrays that allow vertical flow through backside pore. (B) Schematic of channel architecture for PDMS-based microfluidic perfusion layer (top-down view) designed to distribute incoming fluid from a syringe pump across the sensor array. (C) Scanning electron microscope (SEM) image of the microfluidic-tubing interface and channel openings into the culture well for the section of perfusion layer highlighted in the inset. (D) Magnified SEM image of microfluidic channel openings for fluid infusion into the culture well from the tubing and syringe pump. (E) Top and (F) side view images of the fully assembled chip with the microfluidic layer, perfusion tubing, and PDMS-based outlet drain beneath the PCB.

microfluidic perfusion layer made of poly(dimethylsiloxane) (PDMS) that receives flow from a syringe pump at a controlled rate during cell capture. The perfusion layer divides the applied fluid through bilaterally symmetric branching channels to the sensor array, and Figure 2B presents the design of the microfluidic channels.

Fabrication of the microfluidic distributive channel perfusion layer started with creation of a negative mold of the desired channels using SU-8 50 photoresist (Microchem; Newton, MA). SU-8 50 was spun on a 4 in. silicon wafer to a height of 50 $\mu$m and was prebaked in two steps: 10 min at 65 °C and then 30 min at 95 °C. The wafer was exposed to a mask defining the fluidic channels, creating the negative mold, followed by a two-step postexposure bake: 1 min at 65 °C and then 10 min at 95 °C. The resulting mold is developed in SU-8 developer for 2 min at room temperature, rinsed with isopropyl alcohol, and hard-baked at 125 °C for 15 min. PDMS, mixed at a ratio of 1:10 curing agent to prepolymer, was poured over the negative mold, degassed, and allowed to cure between 2 and 16 h at 70 °C. Individual perfusion layers were cut from the polymerized PDMS, and a "corner punch" technique created all inlets and outlets.

Figure 2C depicts the corner punch used to anchor the microfluidic tubing and supply fluid through the microchannels. The microfluidic perfusion layer was first punctured from the patterned side with a 1 mm dermal biopsy punch, creating a vertical channel at the patterned inlet with a depth of half the PDMS thickness. The second channel is created in a single, angle-changing motion that starts from the side to meet the vertical channel using the same 1 mm biopsy punch while slightly deforming the PDMS to expel the material punched from both channels. A PDMS thin film is covalently bonded to the patterned piece, thus creating a sealed, embedded channel. The PDMS layers are bonded through oxygen plasma activation in a barrel etcher followed by a 70 °C bake for 15 min. A 6 mm dermal biopsy punch is then pressed through the 4 mm thick PDMS microfluidic system to define the culture chamber and open the microfluidics into the culture well (Figure 2D). Finally, the PDMS-based well, with embedded microfluidics, is sealed to the MEMS sensor array, following oxygen plasma activation, alignment, and heating (Figure 2, panels E−F). PTFE ultramicrobore tubing (Cole-Parmer; Vernon Hills, IL) makes fluidic connections between the chip and syringe pumps; the curvature of the corner punch assists in retaining the tubing in place while providing a good seal (Figure 2, panels E−F). A Harvard Apparatus PicoPlus syringe pump (Holliston, MA) delivers constant stream of fluid into the system through a T-connector to split the flow for equal distribution to both fluidic inlets.

**Fluid Flow Modeling.** We modeled the velocity characteristics of the flow around the sensor and through the backside pore using the finite element method (FEM). Simulation of steady-state incompressible flow in the system used the Navier−Stokes equations and the geometry of a single sensor and channel in COMSOL Multiphysics 3.5a (COMSOL; Burlington, MA). Boundary conditions for the incompressible Navier−Stokes equations included: no slip at the interface with pore walls and the sensor, a set velocity uniform across the inlet, and a zero-pressure condition at the outlet with no viscous stress. We computed velocity fields for three flow rates: 2, 4, and 8 $\mu$L/min. This rate of total flow delivered to all sensors was converted to velocity at the inlet of each individual channel, assuming even distribution between sensors and a uniform velocity at the inlet.

**Capture Efficiency Characterization.** We characterized the capture efficiency of the vertical flow sensor and compared with the previous generation of sensor design, which included platforms suspended over shallow pits without microfluidics for cell measurements in a ~100 $\mu$L static well. We will refer to these older sensors as "pit" sensors throughout the rest of the text. Aqueous solutions of 15 $\mu$m polystyrene beads in phosphate buffered saline (PBS) with bead densities of 9000 and 18000 beads per 28 mm$^2$ area were evenly mixed and dispersed onto the sensor array. Beads in solution settled for 10 min prior to sealing the chamber with a glass coverslip. For each bead density, the syringe pump forced PBS through the PDMS microfluidic channel system for 30 min at the specified rate (2, 4, and 8 $\mu$L/min). For pit sensors, which receive no flow, beads settled in a static bath for 30 min. We monitored bead capture through images acquired with a Spot flex monochrome camera (Diagnostic Instruments; Sterling Heights, MI) attached to an Olympus BX51 upright fluorescent microscope (Olympus America Inc.; Center Valley, PA) at an acquisition rate of one image per minute for a 30 min capture period. We repeated the experiments three times for each flow rate and bead density, for a total of 24 experiments.

**Cell Culture and Mass Measurements.** Following previously established protocols,[20] we isolated cells from the enzymatically digested hippocampus of EGFP-actin mice (C57BL/6-Tg(CAG-EGFP)1Osb/J), Jackson Laboratories; Bar Harbor, ME). Mice were used in accordance with protocols established by the University of Illinois Institutional Animal Care and Use Committee and in accordance with all state and federal regulations. Cells were maintained in supplemented Hibernate-A or Neurobasal-A (Invitrogen; Carlsbad, CA) supplemented with 0.5 mM L-glutamine, Gem21 NeuroPlex (Gemini Bio-Products; West Sacramento, CA), 100 units/mL penicillin and 0.1 mg/mL streptomycin under standard culture conditions at 37 °C during growth measurements. Neurobasal and Hibernate are defined media formulations optimized for enriching neuronal growth at low densities and selecting against most mitotic cells.[21,22]

Mass measurement of cells relies on estimating the resonant frequency shift between empty and loaded sensors, a process that is well-characterized,[6,7] and will only be briefly described here (Figure 3). Resonant frequency is determined through electromagnetic actuation of the sensors and concurrent velocity measurements with a laser Doppler vibrometer (LDV) system housed on a Zeiss Axiotech Vario upright microscope (Carl Zeiss AG; Jena, Germany). Prior to seeding the sensors with cells, two measurements are made on the empty sensors. First, the resonant frequency of each sensor in air is measured to determine the effective spring constant for each device, assuming negligible damping. Second, the resonant frequency of the sensors in cell culture media is measured to account for the change in resonant frequency from damping and hydrodynamic loading.[23] Finally, dissociated cells are seeded and captured onto the sensor array and the resulting resonant frequencies of the sensors loaded with cells are measured. Measuring these frequencies allows for the extraction of the adhered mass of the cells on the platform from the final measured resonant frequency of the loaded sensors.

**Volume Measurements and Immunocytochemistry.** Following mass measurement, cells were fixed (4% paraformaldehyde in PBS, 30 min) for volume estimation with
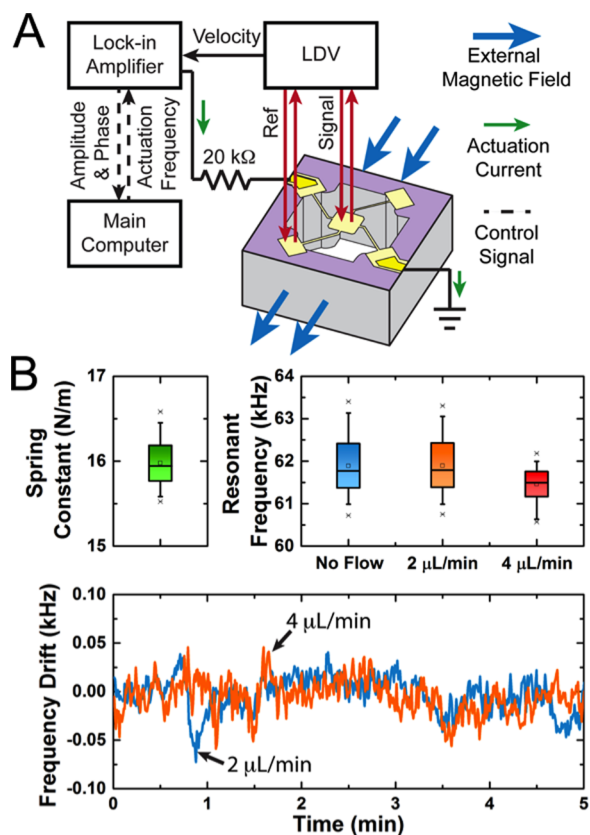
**Figure 3.** Operation and characterization of vertical flow resonant sensor array. (A) Overview of the mass measurement setup. (B) Distribution of the sensor spring constant, a sensor array fabricated with vertical flow channels; distribution of the sensor resonant frequency while submerged in fluid and subject to different applied flow rates; and the variation in sensor resonant frequency with flow applied.

confocal microscopy and cellular identification through immunocytochemistry. The volume of measured cells was obtained using a Zeiss LSM 700 laser scanning confocal microscope with an argon laser (488 nm) and a Plan-Apochromat 20×/0.8 objective (Carl Zeiss Microscopy GmbH; Jena, Germany). Confocal image stacks (Z-stacks) with a $0.63 \times 0.63 \times 0.65 \ \mu m^3$ voxel size were acquired for cell volume calculations using Amira 5.4.1 (Visualization Sciences Group; Mérignac, France).

Cellular identities of neurons were achieved using immunocytochemistry. Cells on sensors were permeabilized with 0.25% Triton-X 100 in PBS for at least 5 min. Samples were blocked from nonspecific antibody binding with 5% bovine serum albumin in PBS, followed by rabbit polyclonal primary antibody incubation for the neuronal marker micro-tubule associated protein-2 (MAP2) (1 h, room temperature). Secondary antibody incubation (goat-anti rabbit, Alexa 568) was performed (1 h, room temperature) prior to imaging with the Spot Flex camera on upright microscope.

## ■ RESULTS AND DISCUSSION

We fabricated MEMS resonant pedestal mass sensors with vertical flow microfluidic pores etched through the wafer. This sensor array enables fluid-exchange during mass measurements without interruption, thereby enabling a greater variety of studies than previously available.[6,9,10] This new on-chip microfluidic system allows for delivery of cells, culture media, and chemical agents to the cells on sensors, while providing a method for removing unwanted cells from the sensor springs to improve sensor measurement yield. Figure 1 shows scanning electron microscope (SEM) images of the fabricated sensor with a backside pore designed to accommodate constant fluid flow. Figure 1H shows a single sensor, which consists of a pedestal suspended by four beam springs over the backside pore. Etching completely through the wafer backside produces
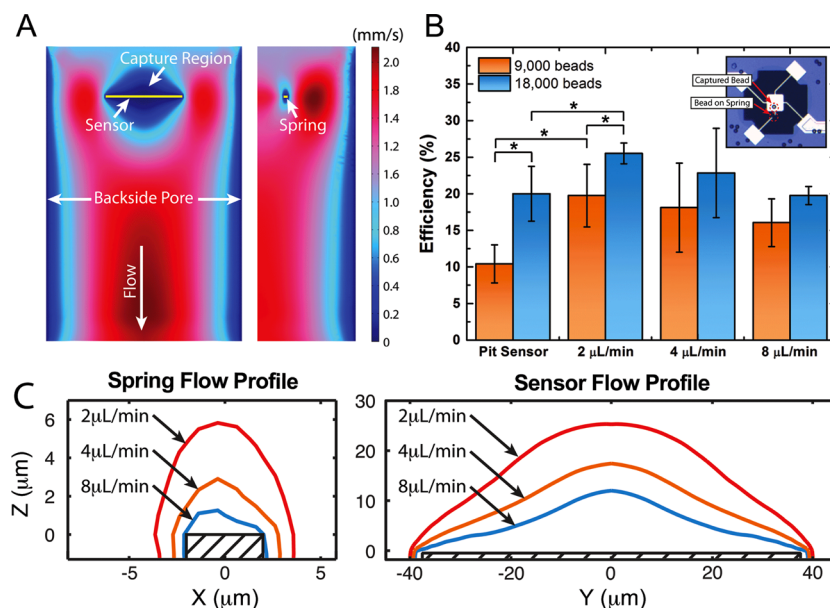


**Figure 4.** Fluidic modeling and experimental sensor capture efficiency. (A) Simulation of the microfluidic vertical flow field comprising the fluid-filled space and the MEMS sensor platform or spring (top of image). (B) Experimental capture efficiency comparison of the no flow pit sensor with the vertical flow sensor, which shows approximately 100% increase in capture efficiency; inset shows an example of beads captured on platforms and springs. (C) Simulation results of the capture region area/volume for the different applied flow rates from 2 to 8 $\mu L$/min on the springs (left) and the sensor (right).
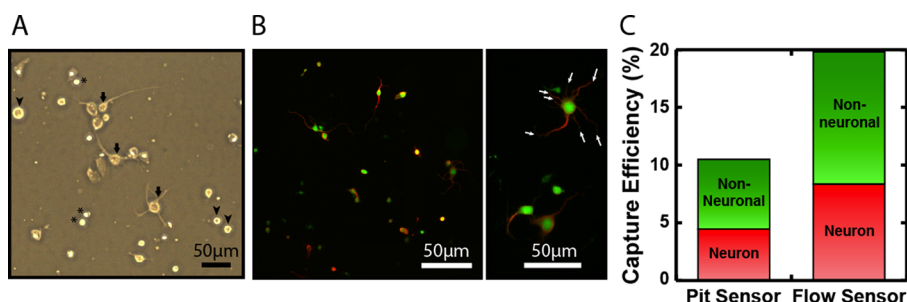
**Figure 5.** Cell capture analysis for heterogeneous populations of primary EGFP-transgenic mouse brain cells on MEMS resonant mass sensor arrays. (A) Phase contrast microscopy and (B) fluorescence microscopy images of 15-hour, age-matched cultures of EGFP-actin transgenic mouse primary hippocampal neurons in flasks and on silicon chips for population analysis. (C) With the use of the primary neuron population characteristics with expected capture efficiency from microbead experiments, we predict the capture efficiency of neurons to be 4.5% for the pit sensor and 8.4% for the flow sensor.

the pores (Figure 1I) that constitute an on-chip microfluidic system when combined with a horizontal PDMS-based, embedded microfluidic perfusion layer (Figure 2). Each chip contains 81 sensors (arranged in a 9 × 9 array) for high measurement throughput (Figure 1J).

Cell mass measurements require operation of the sensors in the first resonance mode to ensure uniform mass sensitivity where the average platform vibrates vertically at $167 \pm 10$ kHz in-air and $68 \pm 5$ kHz in-liquid, owing to an average spring constant of $18 \pm 2$ N/m (Figure 3). These values compare well with those of the previous generation "pit" sensor, which exhibited $152 \pm 7$ kHz and $63 \pm 3$ kHz in-air and in-liquid resonant frequencies, respectively. The difference in resonant frequency between the vertical flow field sensors introduced here and the pit sensors is due to the variation in wafer and sensor layer thicknesses during manufacturing and micro-fabrication.[24]

It is critical that the incorporation of flow-exchange capabilities (sensor structure and flow fields) do not affect the sensor measurements. Mass is estimated through measurement of the device resonant frequency using an LDV system (Figure 3A). Figure 3B shows the range in spring constants of all mass sensors on a typical chip and their resonant frequencies at different flow rates. Essentially, there is less than 1% deviation in the resonant frequency with applied flow rates of 2 and 4 μL/min compared with no flow resonant frequency. In comparison to our previous sensor arrays (frequency drift = 100−200 Hz/day),[6] Figure 3B shows that resonant frequency drift of the new sensor is similar (slope of drift is 80 Hz over 24 h) in the presence of media flow at both 2 and 4 μL/min. Much higher flow rates may be desirable for certain applications, though it is likely that the increased hydrodynamic loading at higher flow rate will alter the resonant frequency and quality factor,[23] which should be considered during experimental design.

We performed simulations using finite element analysis to calculate and visualize the flow velocity profiles through the channel (Figure 4A). The fluid velocity around the sensor pedestal and springs is of particular interest since it will govern the cell capture characteristics. Modeling data shows a low velocity field above the pedestal sensor, which is also the cell attachment area, and this low velocity field appears to remain unaffected by media flow. In contrast, high velocity fields exist around the springs to deter cell attachment.

To demonstrate improvements in capture efficiency over the previous sensor technology, we seeded beads on both new vertical flow sensors and on the pit sensor array (an array

without flow capabilities). Figure 4B shows the capture efficiency of the beads on the pit sensor versus the flow sensor with various flow rates, along with an example image of a captured bead. Two-way ANOVA tested the dependence of capture efficiency on both seed density and flow rate. We found capture efficiency exhibits a statistical dependence on flow rate ($p = 0.016$), with a maximum occurring at 2 μL/min. There is also dependence on seed density ($p = 0.001$), with maximum capture efficiency at 18000 beads per 28 mm² diameter.

Figure 4C shows "capture regions" around the springs and sensor defined by thresholding the simulated velocity field at 5 μm/s. These regions help explain why the apparent maximum efficiency appears to occur at 2 μL/min and not at higher flow rates. The capture zone around the spring for the 2 μL/min suggests that an object larger than approximately 5 μm will be affected and prevented from settling on the springs. While the capture zone shrinks with higher flow rate, this should have no additional effect on the beads used in this experiment, which are 15 μm in diameter. However, the increased flow rate also reduces the capture region of the sensors. This will have the effect of dragging beads off the sensors; especially those not captured near the center.

In practice, the number of useable sensors with viable neurons is further reduced from the stochastic capture rate due to the presence of other cells in the sample. While the hippocampus is a structurally defined region of brain tissue that is easy to excise and dissociate for developmental studies of neuronal cells in vitro,[25] the process of cellular extraction yields a mixed population of neurons, glial cells, microglia, and endothelial cells.[22] Defined media formulations have been produced to sustain neurons in culture, while selecting against non-neuronal and mitotic cell types.[22] In addition to a media-dependent population selection, neurons in culture develop at different rates dependent upon the stage of in situ cell development at the time of neuronal isolation.[26] Therefore, different maturation rates, or durations of "time-to-polar-ization," will also be observed.

To better understand the probability of capturing neurons, particularly differentiating neurons and their non-neuronal cellular counterparts, we performed morphometric and immunocytochemical analyses of age-matched cultures to characterize the cellular populations present in our experiments (Figure 5). From phase contrast imaging of the cell population in culture, we predict that living adherent cells (spherical or ramified) will be approximately 40% of all cells captured on the sensors in our studies, while approximately 20% of the living cells (8% of total cells) will have ramified processes reminiscent
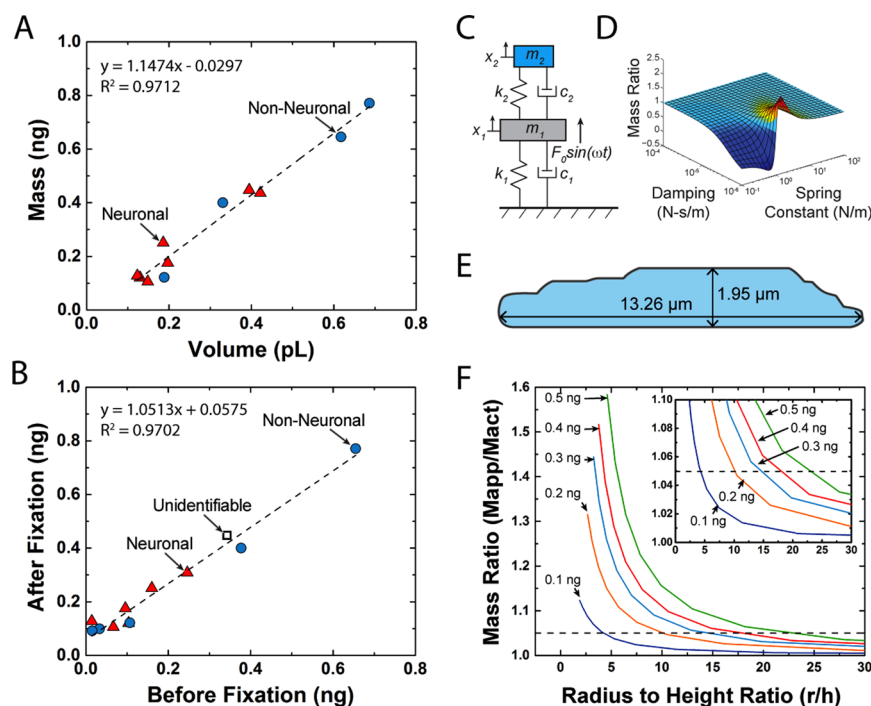
**Figure 6.** (A) Mass of cells estimated with resonant sensors shows a strong linear relationship with estimates of cell volume obtained through confocal microscopy. Red ▲ mark neuronal cells and blue ● mark non-neuronal cells, while an unidentifiable cell is indicated by □. (B) The apparent mass of brain cells after fixation is 1.05 times greater than before fixation. (C) Schematic of dynamic model demonstrating the two-degree-of-freedom (2DOF) mass-spring-damper system. (D) An overview three-dimensional plot showing how stiffness and viscosity affect the result of the 2DOF system. (E) Cross-section of a neuron, indicating the height and width values, which was reconstructed in Amira for 3D data visualization and analysis. (F) Shows the apparent mass from the sensor to the actual mass ratio and how that ratio is directly affected by the shape of the cell.

of neuronal growth after 15 h in culture (Figure 5A). Further, immunocytochemical staining of the culture population revealed that neurons account for 60% of the living cells in culture, while the remaining 40% are non-neuronal cells, such as glia (Figure 5B).[27] Figure 5C presents the predicted efficiency of capturing living brain cells on the platform sensors, derived by multiplying the results from the observations in culture with the capture efficiency from the microbead experiments. The capture efficiency of neurons on pit sensors is estimated at 4.5%, while flow sensors should exhibit 8.4% capture efficiency. With dependence on the cell type of interest, experimental parameters will need to be optimized for capturing adherent cells, bearing in mind that flow velocity regions scale appropriately. The resulting optimized capture efficiency will also depend on factors such as cell geometry, buoyancy, adhesion, and viscoelasticity that can influence retention on the sensor area. For example, cell adhesiveness, a topic of intense research for decades,[28−30] is cell- and substrate-dependent;[31] therefore, cell capture dynamics will vary, depending on the population under investigation.

Dissociated cells from the mouse hippocampus were seeded on sensor arrays for mass measurements at a single time point. Cells were then fixed for immunolabeling and confocal microscopy to estimate cell volume. Figure 6A plots the cell mass and volume of each cell measured and marked by the identified cell type, where the measured mass ranges from 0.1 to 0.9 ng. The slope of the linear fit indicates the density of the cells to be approximately 1.15 ± 0.04 g/mL, which is similar to reported ranges for nonadherent murine lymphocytes and human erythrocytes.[5] The Pearson linear correlation test of mass and volume returned a $R^2$ of 0.97 and p-value < 0.001,

indicating that the strong correlation between the two measures is statistically significant.

We also repeated each mass measurement after fixation, and Figure 6B shows the comparison of measured mass before and after fixation. This type of fixation measurement was previously used to demonstrate how the apparent measured mass is a function of the viscoelasticity of the measured cell,[6] with the measured mass of soft materials deviating from the actual mass. This apparent mass difference is explained by a two-degree-of-freedom (2DOF) dynamic system modeling the cell mass oscillating out-of-phase with the platform sensor (Figure 6C).[10] This oscillation causes an additional resonant frequency shift, and Figure 6D depicts how this changes the apparent mass based on material properties. Since fixation causes a significant stiffening of tissue,[32,33] it is expected that the apparent mass measured before and after fixation should not be the same. However, from the slope of the fit line in Figure 6B, we observed an apparent mass ratio of approximately 1.05, which is lower than described in our previous study on a different cell type (human cancer cell line).[6] While the previously reported neuron stiffness of 1 kPa[34] could produce a more significant deviation, it should be noted that the effective stiffness and damping ratio in Figure 6 (panels C and D) depend not only on the material properties but also on the shape of the object. Treating the cell as a cylinder and using the elastic modulus of 1 kPa and assuming a viscosity of 1 mPa s, we explored how the low profile of the brain cells (Figure 6E) greatly affects the apparent mass ratio estimated from the fixation measurement (Figure 6F). As a cell gets shorter and wider, the apparent mass ratio approaches unity. The adherent cells investigated had a very high radius to height ratio (>5), and thus, the apparent mass exhibited only a small deviation from actual mass.
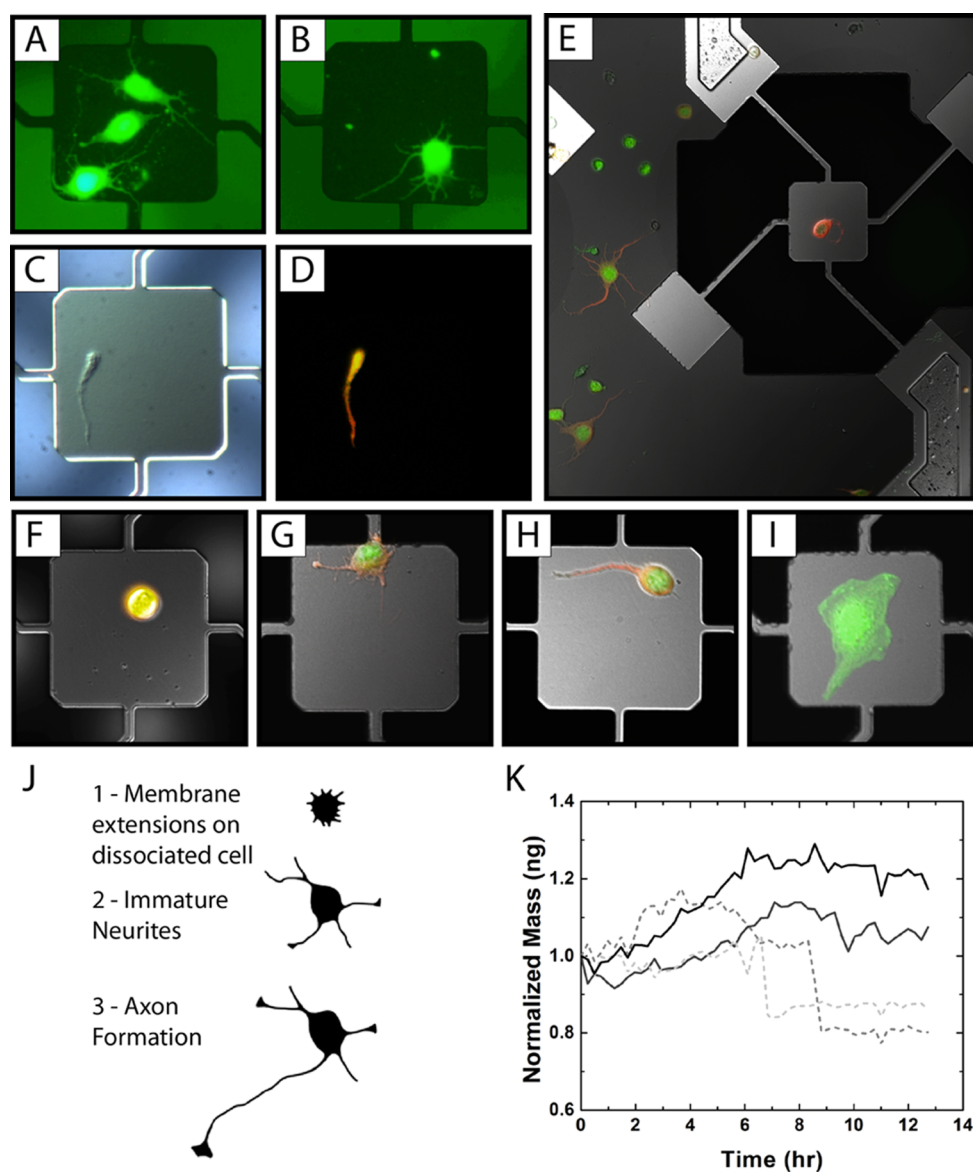
**Figure 7.** Mass and growth of neurons and glial cells measured by MEMS resonant mass sensors. The heterogeneous population of seeded cells leads to the capture of neuronal clusters or individual neurons captured on sensors (A–B) or even subcellular fragments, such as dendrites identified by size and high MAP2 expression (C–D). The captured neurons vary in development and differentiation states ranging from undifferentiated to polarized morphologies (E–H) and are easily distinguished from (I) suspected glial cells. (J) Pictographic summary characteristic of early neuronal growth and differentiation, redrawn, and modeled after previous descriptions.[35] (K) Mass of four individual cells measured with vertical flow resonant sensors. Putative neuronal growth (solid lines) and cell selection and death (dashed lines) are observable from measured growth profiles.

The prototypical neuronal marker MAP2 identifies somato-dendritic structures of neurons. MAP2 immunolabeling is used to characterize hippocampal neurons of EGFP transgenic mice, following mass measurement. Immature neurons differentiate by extending primary neurites, which then differentiate into an axon (longest process) and dendrites. While conventional culture protocols implement cell adhesion molecules for neuronal attachment, neurons show prototypical growth, differentiation, and adhesion on native silicon oxide surfaces. Figure 7 (panels A–I) demonstrates that all stages of neuronal development are present on our chips and sensors. Even disconnected dendrites are observable in culture adhering to the sensor surface.

Finally, to demonstrate the functionality of this MEMS mass sensor array for investigating neuronal cell growth, we performed preliminary growth measurements of primary, dissociated postnatal mouse cells from the hippocampus of the EGFP-expressing transgenic mouse. Methods for culturing primary neurons in defined media render nearly pure neuronal populations at about 4 days in culture. Figure 7J shows a schematic representation of early prototypical neuronal growth and differentiation in vitro. Figure 7K shows growth profiles for 4 cells captured on the vertical flow MEMS sensor array. After initial seeding, non-neuronal mitotic cells, which are abundant in primary cultures, begin to die off, while neurons grow and differentiate. Two of the cells exhibit growth, while the remaining two cells show an abrupt mass decrease without recovery as early as 7 h in vitro, and may mark the death of non-neuronal cells. Previous studies using these sensors show that the apparent mass increase observed by the pedestal sensor represents true cell growth.[6]

Mass growth profiles of primary neurons in culture have not been previously explored; our preliminary data shows an increase in mass growth followed by a plateau, which could be reminiscent of the internal commitment to axonal specification of neurons. The establishment of neuronal polarity (i.e., the extension and differentiation of neurites into axons and dendrites) is very well-defined.[35] Dissociated neurons in vitro begin to send out immature neurites (typically 3−5 neurites), which remain approximately equal in length until one of the processes becomes comitted to form an axon. After axonal specification, the axon exhibits robust growth to become the longest process, while the remaining processes commit to a dendritic fate and exhibit a slower growth rate. Our mass sensor provides an aggregate measurement of neuronal growth, or non-neuronal death, and is not capable of measuring the growth of each process. The advancements and improvements made to the sensor and demonstrated within this body of work allow for the measurement of the physical properties of individual neurons and can enable investigations of neuronal growth and differentiation. Future studies can couple mass measurements with other methods for capturing additional information on cellular morphology to better resolve growth with respect to specific cell state and axonal process development.

## CONCLUSION

To overcome the challenges associated with investigating heterogeneous cell populations in primary culture with MEMS mass sensors, we designed and fabricated a platform resonant sensor array with backside pore and integrated microfluidics. The on-chip microfluidic system allows for the constant supply of cellular growth media and also provides the means to increase removal of objects captured on sensor springs to improve capture efficiency and measurement yield. Characterization of device capture efficiency demonstrated a 2-fold increase over the previous generation sensor that did not allow for fluid flow. We used the resonant sensor with vertical flow fields to measure the mass of heterogeneous cells harvested and dissociated from the mouse hippocampus. The measured mass, ranging from 0.1 to 0.9 ng, shows strong agreement with independent measurements of cell volume from confocal microscopy and reveals the cell density to be approximately 1.15 g/mL. Growth profiles of immature neurons correspond with the characteristic developmental process of neuronal development, while growth profiles of non-neuronal cells reveal death in defined media as early as 7 h in vitro. Further studies of neuronal growth dynamics with this MEMS resonant sensor array may allow for the study of neuronal differentiation and selection with high measurement yield.

## AUTHOR INFORMATION

**Corresponding Author**
*E-mail: rbashir@illinois.edu.

**Notes**
The authors declare no competing financial interest.

## REFERENCES

(1) Lindstrom, S.; Andersson-Svahn, H. *Lab Chip* **2010**, *10*, 3363−3372.
(2) Park, K.; Jang, J.; Irimia, D.; Sturgis, J.; Lee, J.; Robinson, J. P.; Toner, M.; Bashir, R. *Lab Chip* **2008**, *8*, 1034−1041.
(3) Weng, Y. C.; Delgado, F. F.; Son, S.; Burg, T. P.; Wasserman, S. C.; Manalis, S. R. *Lab Chip* **2011**, *11*, 4174−4180.
(4) Bryan, A. K.; Goranov, A.; Amon, A.; Manalis, S. R. *Proc. Natl. Acad. Sci. U.S.A.* **2010**, *107*, 999−1004.
(5) Grover, W. H.; Bryan, A. K.; Diez-Silva, M.; Suresh, S.; Higgins, J. M.; Manalis, S. R. *Proc. Natl. Acad. Sci. U.S.A.* **2011**, *108*, 10992−10996.
(6) Park, K.; Millet, L. J.; Kim, N.; Li, H.; Jin, X.; Popescu, G.; Aluru, N. R.; Hsia, K. J.; Bashir, R. *Proc. Natl. Acad. Sci. U.S.A.* **2010**, *107*, 20691−20696.
(7) Park, K.; Namjung, K.; Morisette, D. T.; Aluru, N. R.; Bashir, R. *JMEM* **2012**, *21*, 702−711.
(8) Godin, M.; Delgado, F. F.; Son, S. M.; Grover, W. H.; Bryan, A. K.; Tzur, A.; Jorgensen, P.; Payer, K.; Grossman, A. D.; Kirschner, M. W.; Manalis, S. R. *Nat. Methods* **2010**, *7*, 387−U70.
(9) Millet, L. J.; Corbin, E. A.; Free, R.; Park, K.; Kong, H.; King, W. P.; Bashir, R. *Small* **2012**, *8*, 2555−2562.
(10) Corbin, E. A.; Millet, L. J.; Pikul, J. H.; Johnson, C. L.; Georgiadis, J. G.; King, W. P.; Bashir, R. *Biomed. Microdevices* **2013**, *15*, 311−319.
(11) Millet, L. J.; Gillette, M. U. *Yale J. Biol. Med.* **2012**, *85*, 501.
(12) Millet, L. J.; Gillette, M. U. *Trends Neurosci.* **2012**, DOI: 10.1016/j.tins.2012.09.001.
(13) Roy, J.; Kennedy, T. E.; Costantino, S. *Lab Chip* **2013**, *13*, 498−508.
(14) Park, K.; Bashir, R. In *Transducers*; IEEE: Denver, CO, 2009; pp 1956−1958.
(15) Corbin, E. A.; Dorvel, B. R.; Millet, L. J.; King, W. P.; Bashir, R. *Lab Chip* **2014**, *14*, 1401−1404.
(16) Vitriol, E. A.; Zheng, J. Q. *Neuron* **2012**, *73*, 1068−1081.
(17) Yamamoto, H.; Demura, T.; Morita, M.; Banker, G. A.; Tanii, T.; Nakamura, S. *J. Neurochem.* **2012**, *123*, 904−910.
(18) Romanova, E. V.; Fosser, K. A.; Rubakhin, S. S.; Nuzzo, R. G.; Sweedler, J. V. *FASEB J.* **2004**, *18*, 1267−1269.
(19) Millet, L. J.; Stewart, M. E.; Nuzzo, R. G.; Gillette, M. U. *Lab Chip* **2010**, *10*, 1525−1535.
(20) Millet, L. J.; Collens, M. B.; Perry, G. L. W.; Bashir, R. *Integr. Biol.* **2011**, *3*, 1167−1178.
(21) Millet, L. J.; Stewart, M. E.; Sweedler, J. V.; Nuzzo, R. G.; Gillette, M. U. *Lab Chip* **2007**, *7*, 987−994.
(22) Brewer, G. J.; Torricelli, J. R.; Evege, E. K.; Price, P. J. *J. Neurosci Res.* **1993**, *35*, 567−576.
(23) Park, K.; Shim, J.; Solovyeva, V.; Corbin, E.; Banerjee, S.; Bashir, R. *Appl. Phys. Lett.* **2012**, *100*, 154107.
(24) Park, K.; Millet, L.; Kim, N.; Li, H.; Hsia, K.; Aluru, N.; Bashir, R. In *Solid-State Sensors, Actuators and Microsystems Conference (Transducers), 2011 16th International*; IEEE: Piscataway, NJ, 2011; pp 759−762.
(25) Kaech, S.; Banker, G. *Nat. Protoc.* **2007**, *1*, 2406−2415.
(26) Fletcher, T. L.; Banker, G. A. *Dev. Biol.* **1989**, *136*, 446−454.
(27) Chang, J. C.; Brewer, G. J.; Wheeler, B. C. *Journal of Neural Engineering* **2006**, *3*, 217.
(28) Bangham, A.; Pethica, B. *Proceedings of the Royal Physical Society of Edinburgh* **1960**, 43−50.
(29) Curtis, A. S. *Exp. Cell Res.* **1961**, *Suppl 8*, 107−122.
(30) Pierres, A.; Benoliel, A. M.; Touchard, D.; Bongrand, P. *Biophys. J.* **2008**, *94*, 4114−4122.
(31) McCarthy, K. D.; Partlow, L. M. *Brain Res.* **1976**, *114*, 391−414.
(32) Hutter, J.; Chen, J.; Wan, W.; Uniyal, S.; Leabu, M. *J. Microsc.* **2005**, *219*, 61−68.
(33) Braet, F.; Rotsch, C.; Wisse, E.; Radmacher, M. *Appl. Phys. A: Mater. Sci. Process.* **1998**, *66*, S575−S578.

(34) Lu, Y.-B.; Franze, K.; Seifert, G.; Steinhäuser, C.; Kirchhoff, F.; Wolburg, H.; Guck, J.; Janmey, P.; Wei, E.-Q.; Käs, J. *Proc. Natl. Acad. Sci. U.S.A.* **2006**, *103*, 17759−17764.

(35) Dotti, C. G.; Sullivan, C. A.; Banker, G. A. *J. Neurosci.* **1988**, *8*, 1454−1468.